

LOVIS ANDERSON¹, MARK TURNER², THORSTEN KOCH³

Generative deep learning for decision making in gas networks

¹  0000-0002-4316-1862

²  0000-0001-7270-1496

³  0000-0002-1967-0077

Zuse Institute Berlin
Takustr. 7
14195 Berlin
Germany

Telephone: +49 30-84185-0
Telefax: +49 30-84185-125

E-mail: bibliothek@zib.de
URL: <http://www.zib.de>

ZIB-Report (Print) ISSN 1438-0064
ZIB-Report (Internet) ISSN 2192-7782

Generative deep learning for decision making in gas networks

Lovis Anderson, Mark Turner, Thorsten Koch

February 4, 2021

Abstract

A decision support system relies on frequent re-solving of similar problem instances. While the general structure remains the same in corresponding applications, the input parameters are updated on a regular basis. We propose a generative neural network design for learning integer decision variables of mixed-integer linear programming (MILP) formulations of these problems. We utilise a deep neural network discriminator and a MILP solver as our oracle to train our generative neural network. In this article, we present the results of our design applied to the transient gas optimisation problem. With the trained network we produce a feasible solution in 2.5s, use it as a warm-start solution, and thereby decrease global optimal solution solve time by 60.5%.

1 Introduction

Mixed-Integer Linear Programming (MILP) is concerned with the modelling and solving of problems from discrete optimisation. These problems can represent real-world scenarios, where discrete decisions can be appropriately captured and modelled by the integer variables. In real-world scenarios a MILP model is rarely solved only once. More frequently, the same model is used with varying data to describe different instances of the same problem which are solved on a regular basis. This holds true in particular for decision support systems, which can utilise MILP to provide real-time optimal decisions on a continual basis, see [4] and [40] for examples in nurse scheduling and vehicle routing. The MILPs that these decision support systems solve have identical structure due to both their underlying application and cyclical nature, and thus often have similar optimal solutions. Our aim is to exploit this repetitive structure, and create generative neural networks that generate binary decision encodings for subsets of important variables. These encodings can then be used in a primal heuristic by solving the induced sub-problem following variable fixations. Additionally, the result of the primal heuristic can be used in a warm-start context to help improve solver performance in a globally optimal context. We demonstrate the performance of our neural network (NN) design on the transient gas optimisation problem [38],

specifically on real-world instances embedded in day-ahead decision support systems.

The design of our framework is inspired by the recent development of Generative Adversarial Networks (GANs) [17]. Our design consists of two NNs, a Generator and a Discriminator. The Generator is responsible for generating the binary decision values, while the Discriminator is tasked with predicting the optimal objective function value of the MILP induced by fixing these binary variables to their generated values.

Our NN design and its application to transient gas-network MILP formulations is an attempt to integrate Machine Learning (ML) into the MILP solving process. This integration has recently received an increased focus [7, 16, 43], which has been encouraged by the success of ML integration into other facets of combinatorial optimisation, see [5] for a thorough overview. Our contribution to this intersection of two fields is as follows: We introduce a new generative NN design for learning integer variables of parametric MILPs, which interacts with the MILP directly during training. We also apply our design to a much more difficult and convoluted problem than traditionally seen in similar papers, namely the transient gas transportation problem. This paper is to the best of our knowledge the first successful implementation of ML applied to discrete control in gas-transport.

2 Background and Related Work

As mentioned in the introduction, the intersection of MILP and ML is currently an area of active and growing research. For a thorough overview of Deep Learning (DL), the relevant subset of ML used throughout this article, we refer readers to [18], and for MILP to [1]. We will highlight previous research from this intersection that we believe is either tangential, or may have shared applications to that presented in this paper. Additionally, we will briefly detail the state-of-the-art in transient gas transport, and highlight why our design is of practical importance. It should be noted as-well, that there are recent research activities aiming at the reverse direction, with MILP applied to ML instead of the orientation we consider, see [45] for an interesting example.

Firstly, we summarise applications of ML to adjacent areas of the MILP solving process. [16] creates a method for encoding MILP structure in a bipartite graph representing variable-constraint relationships. This structure is the input to a Graph Convolutional Neural Network (GCNN), which imitates strong branching decisions. The strength of their results stem from intelligent network design and the generalisation of their GCNN to problems of a larger size, albeit with some generalisation loss. [47] take a different approach, and use a NN design that incorporates the branch-and-bound tree state directly. In doing so, they show that information contained in the global branch-and-bound tree state is an important factor in variable selection. Furthermore, they are one of the

few publications to present techniques on heterogeneous instances. [12] show a successful implementation of reinforcement learning for variable selection. [43] show preliminary results of how reinforcement learning can be used in cutting-plane selection. By restricting themselves exclusively to Gomory cuts, they are able to produce an agent capable of selecting better cuts than default solver settings for specific classes of problems.

There exists a continuous trade-off between model exactness and complexity in the field of transient gas optimisation, and as such, there is no standard model for transient gas transportation problems. [31] presents a piece-wise linear MILP approach to the transient gas transportation problem, [8] a non-linear approach with a novel discretisation scheme, and [24] and [26] a linearised approach. For the purpose of our experiments, we use the model of [24], which uses linearised equations and focuses on active element heavy subnetworks. The current research of ML in gas transport is still preliminary. [37] use a dual NN design to perform online calculations of a compressors operating point to avoid re-solving the underlying model. The approach constraints itself to continuous variables and experimental results are presented for a gunbarrel type network. [30] present a NN combined with a genetic algorithm for learning the relationship between compressor speeds and the fuel consumption rate in the absence of complete data. More often ML has been used in fields closely related to gas transport, as in [20], with ML used to track the degradation of compressor performance, and in [35] to forecast demand values at the boundaries of the network. For a more complete overview of the transient gas literature, we refer readers to [38].

Our Discriminator design, which predicts the optimal objective value of an induced sub-MILP, can be considered similar to [3] in what it predicts and similar to [14] in how it works. In the first paper [3], a neural network is used to predict the associated objective value improvements on cuts. This is a smaller scope than our prediction, but is still heavily concerned with the MILP formulation. In the second paper [14], a technique is developed that performs backward passes directly through a MILP. It does this by solving MILPs exclusively with cutting planes, and then receiving gradient information from the KKT conditions of the final linear program. This application of a neural network, which produces input to the MILP, is very similar to our design. The differences arise in that we rely on a NN Discriminator to appropriately distribute the loss instead of solving a MILP directly, and that we generate variable values instead of parameter values with our Generator.

While our discriminator design is heavily inspired from GANs [17], it is also similar to actor-critic algorithms, see [36]. These algorithms have shown success for variable generation in MILP, and are notably different in that they sample from a generated distribution for down-stream decisions instead of always taking the decision with highest probability. Recently, [9] generated a series of coordinates for a set of UAVs using an actor-critic based algorithm, where these coordinates were continuous variables in a MINLP formulation. The independence of separable sub-problems and the easily realisable value function within

their formulation resulted in a natural Markov Decision Process interpretation. For a better comparison on the similarities between actor-critic algorithms and GANs, we refer readers to [36].

Finally, we summarise existing research that also deals with the generation of decision variable values for MIPs. [6, 7] attempt to learn optimal solutions of parametric MILPs and MIQPs, which involves both outputting all integer decision variable values and the active set of constraints. They mainly use Optimal Classification Trees in [6] and NNs in [7]. Their aim is tailored towards smaller problems classes, where speed is an absolute priority and parameter value changes are limited. [29] learn binary warm start decisions for MIQPs. They use NNs with a loss function that combines binary cross entropy and a penalty for infeasibility. Their goal of a primal heuristic is similar to ours, and while their design is much simpler, it has been shown to work effectively on very small problems. Our improvement over this design is our non-reliance on labelled optimal solutions which are needed for binary cross entropy. [11] present a GCNN design which is an extension of [16], and use it to generate binary decision variable values. Their contributions are a tripartite graph encoding of MILP instances, and the inclusion of their aggregated generated values as branching decisions in the branch-and-bound tree, both in an exact approach and in an approximate approach with local branching [15]. Very recently, [32] combined the branching approach of [16] with a novel neural diving approach, in which integer variable values are generated. They use a GCNN both for generating branching decisions and integer variables values. Different to our generator-discriminator based approach, they generate values directly from a learned distribution, which is based on an energy function that incorporates resulting objective values.

3 The Solution Framework

We begin by formally defining both a MILP and a NN. Our definition of a MILP is an extension of more traditional formulations, see [1], but still encapsulates general instances.

Definition 1. *Let $\pi \in \mathbb{R}^p$ be a vector of problem defining parameters. We call the following a MILP parameterised by π .*

$$\begin{aligned}
 \mathbb{P}_\pi := \quad & \min \quad c_1^\top x_1 + c_2^\top x_2 + c_3^\top z_1 + c_4^\top z_2 \\
 & \text{s.t.} \quad A_\pi \begin{bmatrix} x_1 \\ x_2 \\ z_1 \\ z_2 \end{bmatrix} \leq b_\pi \\
 & c_k \in \mathbb{R}^{n_k}, k \in \{1, 2, 3, 4\}, A_\pi \in \mathbb{R}^{m \times n}, b_\pi \in \mathbb{R}^m \\
 & x_1 \in \mathbb{R}^{n_1}, x_2 \in \mathbb{R}^{n_2}, z_1 \in \mathbb{Z}^{n_3}, z_2 \in \mathbb{Z}^{n_4}
 \end{aligned} \tag{1}$$

Furthermore let $\Sigma \subset \mathbb{R}^p$ be a set of valid problem defining parameters. We then

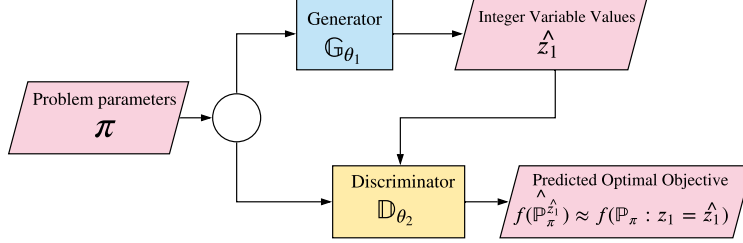


Figure 1: The general design of $\mathbb{N}_{\{\theta_1, \theta_2\}}$

call $\{\mathbb{P}_{\pi} | \pi \in \Sigma\}$ a problem class for Σ .

Note that the explicit parameter space Σ is usually unknown, but we assume in the following to have access to a random variable Π that samples from Σ . In addition, note that c, n_1, n_2, n_3 , and n_4 are not parameterised by π , and as such the objective function and variable dimensions do not change between scenarios.

Definition 2. A k layer NN N_{θ} is given by the following:

$$\begin{aligned}
 N_{\theta} &: \mathbb{R}^{|a_1|} \rightarrow \mathbb{R}^{|a_{k+1}|} \\
 h_i &: \mathbb{R}^{|a_i|} \rightarrow \mathbb{R}^{|a_i|}, \quad \forall i \in \{2, \dots, k+1\} \\
 a_{i+1} &= h_{i+1}(W_i a_i + b_i), \quad \forall i \in \{1, \dots, k\}
 \end{aligned} \tag{2}$$

Here θ fully describes all weights (W) and biases (b) of the network. h_i 's are called activation functions and are non-linear element-wise functions.

An outline of our framework is depicted in Figure 1. The Generator \mathbb{G}_{θ_1} is a NN that takes as input π . \mathbb{G}_{θ_1} outputs values for the variables z_1 , which we denote by \hat{z}_1 . These variable values \hat{z}_1 alongside π are then input into another NN, namely the Discriminator \mathbb{D}_{θ_2} . \mathbb{D}_{θ_2} finally outputs a prediction of the optimal objective function value of \mathbb{P}_{π} with values of z_1 fixed to \hat{z}_1 , namely $\hat{f}(\mathbb{P}_{\pi}^{\hat{z}_1})$. More formally this is:

Definition 3. The generator \mathbb{G}_{θ_1} and discriminator \mathbb{D}_{θ_2} are both NNs defined by the following:

$$\begin{aligned}
 \mathbb{G}_{\theta_1} &: \mathbb{R}^p \rightarrow \mathbb{Z}^{n_3} \\
 \mathbb{D}_{\theta_2} &: \mathbb{R}^p \times \mathbb{Z}^{n_3} \rightarrow \mathbb{R}
 \end{aligned} \tag{3}$$

Furthermore, a forward pass of both \mathbb{G}_{θ_1} and \mathbb{D}_{θ_2} is defined as follows:

$$\hat{z}_1 = \mathbb{G}_{\theta_1}(\pi) \tag{4}$$

$$\hat{f}(\mathbb{P}_{\pi}^{\hat{z}_1}) = \mathbb{D}_{\theta_2}(\hat{z}_1, \pi) \tag{5}$$

The hat notation is used to denote quantities that were approximated by a NN, and $f(\mathbb{P}_\pi)$ refers to the optimal objective function value of \mathbb{P}_π . We use superscript notation to create the following instances:

$$\mathbb{P}_\pi^{\hat{z}_1} = \mathbb{P}_\pi \quad \text{s.t.} \quad z_1 = \hat{z}_1 \quad (6)$$

Note that the values of \hat{z}_1 must be appropriately rounded when explicitly solving $\mathbb{P}_\pi^{\hat{z}_1}$ s.t they are feasible w.r.t. their integer constraints. As such, it is a slight abuse notation to claim that $\mathbb{G}_{\theta_1}(\pi)$ lies in \mathbb{Z}^{n_3}

The goal of this framework is to produce good initial solution values for z_1 , which lead to an induced sub-MILP, $\mathbb{P}_\pi^{z_1}$, whose optimal solution is a good feasible solution to the original problem. Further, the idea is to use this feasible solution as a first incumbent for warm-starting \mathbb{P}_π . To ensure feasibility for all choices of z_1 , we divide the continuous variables into two sets, x_1 and x_2 , as seen in Definition 1. The variables x_2 are potential slack variables to ensure that all generated decisions result in feasible $\mathbb{P}_\pi^{z_1}$ instances. Penalising these slacks in the objective then feeds in naturally to our design, where \mathbb{G}_{θ_1} aims to minimise the induced optimal objectives. For the purpose of our application it should be noted that z_1 and z_2 are binary variables instead of integer. Next we describe the design of \mathbb{G}_{θ_1} and \mathbb{D}_{θ_2} .

3.1 Generator and Discriminator Design

\mathbb{G}_{θ_1} and \mathbb{D}_{θ_2} are NNs whose structure is inspired by [17], as well as both inception blocks and residual NNs, which have greatly increased large scale model performance [42]. We use the block design from Resnet-v2 [42], see Figure 3, albeit with slight modifications for the case of transient gas-network optimisation. Namely, we primarily use 1-D convolutions with that dimension being time. Additionally, we separate initial input streams by their characteristics, and when joining two streams, use 2-D convolutions, where the second dimension is of size 2 and quickly becomes one dimensional again. See Figure 2 for an example of this process. The final layer of \mathbb{G}_{θ_1} contains a softmax activation function with temperature. As the softmax temperature increases, this activation function’s output approaches a one-hot vector encoding. The final layer of \mathbb{D}_{θ_2} contains a softplus activation function. All other intermediate layers of $\mathbb{N}_{\{\theta_1, \theta_2\}}$ use the ReLU activation function. We refer readers to [18] for a thorough overview of deep learning, and to Figure 14 in Appendix A for our complete design.

For a vector $x = (x_1, \dots, x_n)$, the Softmax function with temperature $T \in \mathbb{R}$ (7), ReLU function (8), and Softplus function with parameter $\beta \in \mathbb{R}$ (9) are:

$$\sigma_1(x, T) := \frac{\exp(Tx_i)}{\sum_{j=1}^n \exp(Tx_j)} \quad (7)$$

$$\sigma_2(x_i) := \max(0, x_i) \quad (8)$$

$$\sigma_3(x_i, \beta) := \frac{1}{\beta} \log(1 + \exp(\beta x_i)) \quad (9)$$

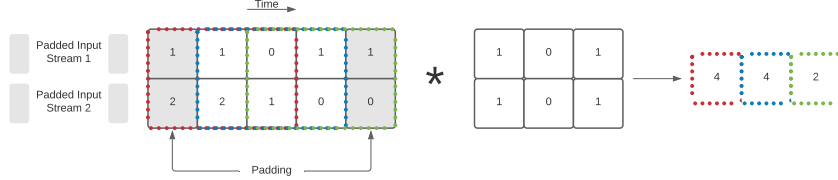


Figure 2: Method of merging two 1-D input streams

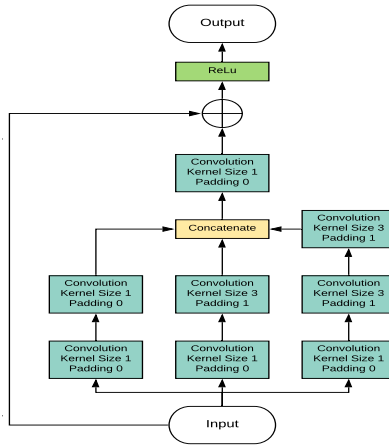


Figure 3: 1-D Resnet-v2 Block Design

We can compose \mathbb{G}_{θ_1} with \mathbb{D}_{θ_2} , as in Figure 1, so that the combined resulting NN is defined as:

$$\mathbb{N}_{\{\theta_1, \theta_2\}}(\pi) := \mathbb{D}_{\theta_2}(\mathbb{G}_{\theta_1}(\pi), \pi) \quad (10)$$

3.2 Interpretations

In a similar manner to GANs and actor-critic algorithms, see [36], the design of $\mathbb{N}_{\{\theta_1, \theta_2\}}$ has a bi-level optimisation interpretation, see [10] for an overview of bi-level optimisation. Here we list the explicit objectives of both \mathbb{G}_{θ_1} and \mathbb{D}_{θ_2} , and how their loss functions represent these objectives.

The objective of \mathbb{D}_{θ_2} is to predict $f(\mathbb{P}_{\pi}^{\hat{z}_1})$, the optimal induced objective values of $\mathbb{P}_{\pi}^{\hat{z}_1}$. Its loss function is thus:

$$L(\theta_2, \pi) := |\mathbb{D}_{\theta_2}(\mathbb{G}_{\theta_1}(\pi), \pi) - f(\mathbb{P}_{\pi}^{\mathbb{G}_{\theta_1}(\pi)})| \quad (11)$$

The objective of \mathbb{G}_{θ_1} is to minimise the induced prediction of \mathbb{D}_{θ_2} . Its loss

function is thus:

$$L'(\theta_1, \pi) := \mathbb{D}_{\theta_2}(\mathbb{G}_{\theta_1}(\pi), \pi) \quad (12)$$

The corresponding bi-level optimisation problem can then be viewed as:

$$\begin{aligned} \min_{\theta_1} \quad & \mathbb{E}_{\pi \sim \Pi} [\mathbb{D}_{\theta_2}(\mathbb{G}_{\theta_1}(\pi), \pi)] \\ \text{s.t.} \quad & \min_{\theta_2} \mathbb{E}_{\pi \sim \Pi} [\mathbb{D}_{\theta_2}(\mathbb{G}_{\theta_1}(\pi), \pi) - f(\mathbb{P}_{\pi}^{\mathbb{G}_{\theta_1}(\pi)})] \end{aligned} \quad (13)$$

3.3 Training Method

For effective training of \mathbb{G}_{θ_1} , a capable \mathbb{D}_{θ_2} is needed. We therefore pre-train \mathbb{D}_{θ_2} . The following loss function, which replaces $\mathbb{G}_{\theta_1}(\pi)$ with prior generated z_1 values in (11), is used for this pre-training:

$$L''(\theta_2, \pi) := |\mathbb{D}_{\theta_2}(z_1, \pi) - f(\mathbb{P}_{\pi}^{z_1})| \quad (14)$$

However, performing this initial training requires generating instances of $\mathbb{P}_{\pi}^{z_1}$. Here we do supervised training in an offline manner on prior generated data.

After the initial training of \mathbb{D}_{θ_2} , we train \mathbb{G}_{θ_1} as a part of $\mathbb{N}_{\{\theta_1, \theta_2\}}$, using samples $\pi \in \Pi$, the loss function (12), and fixed θ_2 . The issue of \mathbb{G}_{θ_1} outputting continuous values for z_1 is overcome by the final layer's activation function of \mathbb{G}_{θ_1} . The softmax with temperature (7) ensures that adequate gradient information still exists to update θ_1 , and that the results are near binary. When using these results to explicitly solve $\mathbb{P}_{\pi}^{z_1}$, we round our result to a one-hot vector encoding along the appropriate dimension.

After the completion of both initial training, we alternately train both NN's using updated loss functions in the following way:

- \mathbb{D}_{θ_2} training:
 - As in the initial training, using loss function (14).
 - In an online fashion, using predictions from \mathbb{G}_{θ_1} and loss function (11).
- \mathbb{G}_{θ_1} training:
 - As explained above with loss function (12).

Our design allows the loss to be back-propagated through \mathbb{D}_{θ_2} and distributed to the individual nodes of the final layer of \mathbb{G}_{θ_1} , i.e., that representing z_1 . This is largely different to other methods, many of which rely on using binary cross entropy loss against optimal solutions of \mathbb{P}_{π} . Our advantage over these is that

the contribution to the objective function we are trying to minimise of each variable decision in z_1 can be calculated. This has an added benefit of generated suboptimal solutions being much more likely to be near-optimal, as they are trained in a manner to minimise the objective rather than copy previously observed optimal solutions.

For our application, transient gas network optimisation, methods for sampling instances currently do not exist. In fact, even gathering data is notoriously difficult, see [28] and [46]. For this reason, we introduce a new method for generating training data in section 5.

4 The Gas Transport Model

To evaluate the performance of our approach, we test our framework on the transient gas optimisation problem, see [38] for an overview of the problem and associated literature. This problem is difficult to solve as it combines a transient flow problem with complex combinatorics representing switching decisions. The natural modelling of transient gas networks as time-expanded networks lends itself well to our framework however, due to the static underlying network and repeated constraints at each time-step.

We use the description of transient gas networks by [24]. The advantages of this description for our framework is a natural separation of z_1 variables, which induce feasible $\mathbb{P}_\pi^{z_1}$ for all choices due to the existence of slack variables in the description. These slack variables are then represented by x_2 in Definition 1. The gas network is modelled as a directed graph $G = (\mathcal{V}, \mathcal{A})$ where \mathcal{A} is the set of arcs representing network elements, e.g. pipes, and the nodes \mathcal{V} represent junctions between adjacent elements. Every arc $a \in \mathcal{A}$ models a specific element with $\mathcal{A} = \mathcal{A}^{\text{pi}} \cup \mathcal{A}^{\text{va}} \cup \mathcal{A}^{\text{rs}} \cup \mathcal{A}^{\text{rg}} \cup \mathcal{A}^{\text{cs}}$, i.e., pipes, valves, resistors, regulators, and compressors. Additionally, the node set \mathcal{V} contains multiple element types, with $\mathcal{V} = \mathcal{V}^{\text{b}} \cup \mathcal{V}^{\text{o}}$ partitioned into boundary and inner nodes respectively. The boundary nodes represent the sources and sinks of the flow network. Thus, flow and pressure forecasts are given for each $v \in \mathcal{V}^{\text{b}}$.

It should be noted that this description focuses on *network stations*, the beating hearts of gas networks. Network stations are commonly located at the intersections of major pipelines and contain nearly all elements, which can be used to control the gas flow. Next, we briefly explain the most important constraints from the model of [24], particularly those which we exploit with our approach. For a full definition of the MILP, please see [24].

As we optimise a transient problem, we deal with a time horizon, namely $\mathcal{T}_0 := \{0, \dots, k\}$. We aim to calculate a network state for each $t \in \mathcal{T} := \mathcal{T}_0 \setminus \{0\}$, i.e. control decisions for all future time steps. As such, the initial gas network state at time 0 contains a complete description of that time step and is immutable. On the other hand all future time steps contain, before optimising, only forecasted pressure and flow values at \mathcal{V}^{b} . We denote $\tau(t)$ as the time difference in seconds

from time step 0.

4.1 Pipe Equations

Pipes constitute the majority of elements in any gas transmission network. The dynamics of flow through pipes are governed by the Euler Equations, a set of nonlinear hyperbolic partial differential equations, see [33]. We consider the isothermal case and discretise as in [23]. Consider the pipe $a = (u, v)$, $a \in \mathcal{A}^{\text{pi}}$, where $u, v \in \mathcal{V}$ are the two incident nodes. We attach a flow-in $q_{u,a,t}$ and flow-out $q_{v,a,t}$ variable to each pipe. Additionally, each incident node has an attached pressure variable, namely $(p_{u,t})$ and $(p_{v,t})$. Moreover, these flow-in, flow-out, and pressure values also appear for each time step. R_s , z_a , and T are assumed to be constant, and D_a , L_a , s_a , A_a , g , and λ_a are themselves constant. The above constant assumptions are quite common in practice [38]. It is only after setting the velocity of gas within each individual pipe, $|v_{w,a}|$ to be constant that all non-linearities are removed however. We do this via a method developed in [23] and seen in [13]. The resulting pipe equations are:

$$p_{u,t_2} + p_{v,t_2} - p_{u,t_1} - p_{v,t_1} + \frac{2R_s T z_a (\tau(t_2) - \tau(t_1))}{L_a A_a} (q_{v,a,t_2} - q_{u,a,t_2}) = 0 \quad (15)$$

$$p_{v,t_2} - p_{u,t_2} + \frac{\lambda_a L_a}{4D_a A_a} (|v_{u,a}| q_{u,a,t_2} + |v_{v,a}| q_{v,a,t_2}) + \frac{g s_a L_a}{2R_s T z_a} (p_{u,t_2} + p_{v,t_2}) = 0 \quad (16)$$

As nodes represent junctions between network elements and thus have no volume in which to store any gas, the flow conservation constraints (17) (18) are required. In the below equations, $d_{v,t}$ represents the inflow resp. outflow of entry and exit nodes in the network at time $t \in \mathcal{T}_0$. Note that network elements that aren't pipes have only one associated flow variable, instead of the in-out flow exhibited by pipes. This is due to them having no volume, and as such no ability to store gas over time, i.e. line-pack.

$$\begin{aligned} & \sum_{(u,w)=a \in \mathcal{A}^{\text{pi}}} q_{w,a,t} - \sum_{(w,v)=a \in \mathcal{A}^{\text{pi}}} q_{w,a,t} \\ + & \sum_{(u,w)=a \in \mathcal{A} \setminus \mathcal{A}^{\text{pi}}} q_{a,t} - \sum_{(w,v)=a \in \mathcal{A} \setminus \mathcal{A}^{\text{pi}}} q_{a,t} + d_{w,t} = 0 \quad \forall w \in \mathcal{V}^{\text{b}} \end{aligned} \quad (17)$$

$$\begin{aligned} & \sum_{(u,w)=a \in \mathcal{A}^{\text{pi}}} q_{w,a,t} - \sum_{(w,v)=a \in \mathcal{A}^{\text{pi}}} q_{w,a,t} \\ + & \sum_{(u,w)=a \in \mathcal{A} \setminus \mathcal{A}^{\text{pi}}} q_{a,t} - \sum_{(w,v)=a \in \mathcal{A} \setminus \mathcal{A}^{\text{pi}}} q_{a,t} = 0 \quad \forall w \in \mathcal{V}^0 \end{aligned} \quad (18)$$

4.2 Operation Modes

Operation modes represent binary decisions in our gas network. We identify the corresponding binary variables with the z_1 variables from our MILP formulation (1). Let \mathcal{O} represent the set of operation modes, and $m_{o,t}^{\text{om}}$ the associated variables. Operation Modes are very important in our modelling context as they describe every allowable combination of discrete decisions associated with *valves* and *compressors*.

4.2.1 Compressors

Compressors are typically set up as a compressor station consisting of multiple compressor units, which represent the union of one single compressor machine and its associated drive. These compressor units are dynamically switched on or off and used in different sequences to meet the current needs in terms of compression ratios and flow rates. Out of the theoretically possible arrangements of compressor units, the set of technically feasible arrangements are known as the *configurations* of a compressor station.

Selecting an operation mode results in fixed configurations for all compressor stations. The binary variables associated with a compressor station $a = (u, v) \in \mathcal{A}^{\text{cs}}$ at time $t \in \mathcal{T}_0$ are $m_{a,t}^{\text{by}}$ (bypass), $m_{a,t}^{\text{cl}}$ (closed), and $m_{c,a,t}^{\text{cf}} \forall c \in \mathcal{C}_a$ (active). \mathcal{C}_a denotes the set of configurations associated to compressor station a available in active mode, where the configuration's operating range is a polytope in space $(p_{u,t}, p_{v,t}, q_{u,a,t})$. The polytope of configuration c is represented by the intersection of half-spaces, $\mathcal{H}_c = \{(\alpha_0, \alpha_1, \alpha_2, \alpha_3) \in \mathbb{R}^4\}$.

$$1 = \sum_{c \in \mathcal{C}_a} m_{c,a,t}^{\text{cf}} + m_{a,t}^{\text{by}} + m_{a,t}^{\text{cl}} \quad (19)$$

$$\alpha_0 p_{c,a,t}^{\text{u-cf}} + \alpha_1 p_{c,a,t}^{\text{v-cf}} + \alpha_2 q_{c,a,t}^{\text{cf}} + \alpha_3 m_{c,a,t}^{\text{cf}} \leq 0 \quad (20)$$

$$\forall (\alpha_0, \alpha_1, \alpha_2, \alpha_3) \in \mathcal{H}_c \quad \forall c \in \mathcal{C}_a$$

Note that the variables in (20) have an extra subscript and superscript compared to those in (15) and (16). This is due to our use of the convex-hull reformulation, see [2]. The additional subscript refers to the configuration in question, and the superscript the mode, with the pressure variables having an additional node identifier. It should also be noted that the continuous variables attached to a compressor station are not fixed by a choice in operation mode or configuration, but rather the operation mode restricts the variables to some polytope.

4.2.2 Valves

Valves decide the allowable paths through a network, and can separate areas, decoupling their pressure levels. They are modelled as an arc $a = (u, v)$, whose discrete decisions can be decided by an operation mode choice. Valves have two

modes, namely open and closed. When a valve is open, similar to a compressor station in bypass, flow is unrestricted and there exists no pressure difference between the valves start and endpoints. Alternatively in the closed mode, a valve allows no flow to pass, and decouples the pressure of the start- and endpoints of the arc. The variable $m_{a,t}^{\text{op}}$ represents a valve being open with value 1 and closed with value 0. The general notation \underline{x} and \bar{x} refer to lower and upper bounds of a variable x . The constraints describing valves are then as follows:

$$p_{u,t} - p_{v,t} \leq (1 - m_{a,t}^{\text{op}})(\bar{p}_{u,t} - \underline{p}_{v,t}) \quad (21)$$

$$p_{u,t} - p_{v,t} \geq (1 - m_{a,t}^{\text{op}})(\underline{p}_{u,t} - \bar{p}_{v,t}) \quad (22)$$

$$q_{a,t} \leq (m_{a,t}^{\text{op}})\bar{q}_{a,t} \quad (23)$$

$$q_{a,t} \geq (m_{a,t}^{\text{op}})\underline{q}_{a,t}. \quad (24)$$

4.2.3 Valid Operation Modes

As mentioned earlier, not all combinations of compressor station configurations and valve states are possible. We thus define a mapping $M(o, a)$ from operation mode $o \in \mathcal{O}$ to the discrete states of all $a \in \mathcal{A}^{\text{va}} \cup \mathcal{A}^{\text{cs}}$

$$M(o, a) := m \text{ where } m \text{ is the mode or configuration of arc } a$$

$$\text{in operation mode } o \quad \forall o \in \mathcal{O} \quad \forall a \in \mathcal{A}^{\text{va}} \cup \mathcal{A}^{\text{cs}}$$

$$\text{with } \quad m \in \{\text{op, cl}\} \text{ if } a \in \mathcal{A}^{\text{va}}$$

$$m \in \{\text{by, cl}\} \cup \mathcal{C}_a \text{ if } a \in \mathcal{A}^{\text{cs}}$$

Using this mapping we can then define a set of constraints for all valid combinations of compressor station and valve discrete states for each $t \in \mathcal{T}$. The variable $m_{o,t}^{\text{om}}$, $o \in \mathcal{O}$ $t \in \mathcal{T}$, is a binary variable, where the value 1 represents the selection of o at time step t .

$$\sum_{o \in \mathcal{O}} m_{o,t}^{\text{om}} = 1 \quad (25)$$

$$m_{a,t}^{\text{op}} = \sum_{o \in \mathcal{O}: M(o,a)=\text{op}} m_{o,t}^{\text{om}} \quad \forall a \in \mathcal{A}^{\text{va}} \quad (26)$$

$$m_{a,t}^{\text{by}} = \sum_{o \in \mathcal{O}: M(o,a)=\text{by}} m_{o,t}^{\text{om}} \quad \forall a \in \mathcal{A}^{\text{cs}} \quad (27)$$

$$m_{a,t}^{\text{cl}} = \sum_{o \in \mathcal{O}: M(o,a)=\text{cl}} m_{o,t}^{\text{om}} \quad \forall a \in \mathcal{A}^{\text{cs}} \quad (28)$$

$$m_{c,a,t}^{\text{cf}} = \sum_{o \in \mathcal{O}: M(o,a)=c} m_{o,t}^{\text{om}} \quad \forall c \in \mathcal{C}_a \quad \forall a \in \mathcal{A}^{\text{cs}} \quad (29)$$

$$m_{o,t}^{\text{om}} \in \{0, 1\} \quad \forall o \in \mathcal{O}.$$

4.3 Flow Directions

Flow Directions define the sign of flow values over the boundary nodes of a network station. With regards to our MILP they are a further set of decision variables. We avoid generating these decisions with our deep learning framework as not all combinations of operation modes and flow directions are feasible. These variables thus exist as integer variables in $\mathbb{P}_{\pi}^{z_1}$, namely as a subset of z_2 , see (1). They are few in number however due to the limited combinations after the operation modes are fixed.

4.4 Boundary Nodes and Slack

Boundary nodes, unlike inner nodes, have a prescribed flow and pressure values for all future time steps. For each boundary node $v \in \mathcal{V}^{\text{b}}$ and $t \in \mathcal{T}$, we have $\sigma_{v,t}^{p+}$ and $\sigma_{v,t}^{p-}$, which capture the positive and negative difference between the prescribed and realised pressure. In addition to these pressure slack variables, we have the inflow slack variables $\sigma_{v,t}^{d+}$ and $\sigma_{v,t}^{d-}$ which act in a similar manner but for inflow. The relationships between the slack values, prescribed values, and realised values can be modelled for each $v \in \mathcal{V}^{\text{b}}$ and $t \in \mathcal{T}$ as:

$$\hat{p}_{v,t} = p_{v,t} - \sigma_{v,t}^{p+} + \sigma_{v,t}^{p-} \quad \forall v \in \mathcal{V}^{\text{b}} \quad (30)$$

$$\hat{d}_{v,t} = d_{v,t} - \sigma_{v,t}^{d+} + \sigma_{v,t}^{d-} \quad \forall v \in \mathcal{V}^{\text{b}} \quad (31)$$

Note that unlike the model from [24], we do not allow the inflow over a set of boundary nodes to be freely distributed according to which group they belong to. This is an important distinction, as each single node has a complete forecast.

4.5 Initial State

In addition to the forecast mentioned in subsection 4.4, we also start our optimisation problem with an initial state. This initial state contains complete

information of all discrete states and continuous values for all network elements at $t = 0$.

4.6 Objective function

The objective of our formulation is to both minimise slack usage, and changes in network operation. Specifically, it is a weighted sum of changes in the active element modes, changes in the continuous active points of operation, and the deviations from given pressure and flow demands. For the exact objective function we refer readers to [24].

5 Computational Experiments

In this section we propose an experimental design to determine the effectiveness of our neural network design approach. We outline how we generate synthetic training data, and show the exact architecture and training method we use for our neural network. Our final test set consists of 15 weeks of real-world data provided by our project partner OGE.

5.1 Data Generation

As mentioned previously, acquiring gas network data is notoriously difficult [28, 46]. Perhaps because of this difficulty, there exists no standard method for generating valid states for a fixed gas network. Below we outline our methods for generating synthetic transient gas instances for training purposes, i.e. generating $\pi \in \Pi$ and artificial z_1 values. For our application of transient gas instances, π is a tuple of a boundary forecast and an initial state.

5.1.1 Boundary Forecast Generation

We consider network stations as our gas network topology. They contain all heavy machinery and at most only short segments of large scale transport pipelines. As such, our gas networks cannot be used to store large amounts of gas. We thus aim to generate balanced demand scenarios, with the requirement described as follows:

$$\sum_{v \in \mathcal{V}^b} \hat{d}_{v,t} = 0 \quad \forall t \in \mathcal{T} \tag{32}$$

The distribution of gas demand scenarios is not well known. Hence we naively assume a uniform distribution, and using the largest absolute flow value found over any node and time step in our real-world data, create an interval as follows:

$$\begin{aligned}
M_q &= \max_{v \in \mathcal{V}^b, t \in \mathcal{T}} |\hat{d}_{v,t}| \\
\hat{d}_{v,t} &\in [-1.05M_q, 1.05M_q]
\end{aligned} \tag{33}$$

In addition to the above, we require three MILP formulation specific requirements. The first is that the absolute difference between the flow values of a node is not too large for any adjacent time steps. Secondly, the sign of the generated flow values must match the attribute of the boundary node, i.e., entry (+), exit (-). Thirdly, the flow values do not differ too largely between boundary nodes of the same *fence group* within the same time step. A fence group is denoted by $g \in \mathcal{G}$, and enforces the sign of all nodes in the group to be identical. These constraints are described below:

$$\begin{aligned}
|\hat{d}_{v,t} - \hat{d}_{v,t-1}| &\leq 200 \quad \forall t \in \mathcal{T}, \quad v \in \mathcal{V}^b \\
\text{sign}(\hat{d}_{v,t}) &= \begin{cases} 1 & \text{if } v \in \mathcal{V}^+ \\ -1 & \text{if } v \in \mathcal{V}^- \end{cases} \quad \forall t \in \mathcal{T}, \quad v \in \mathcal{V}^b \\
|\hat{d}_{v_1,t} - \hat{d}_{v_2,t}| &\leq 200 \quad \forall t \in \mathcal{T}, \quad v_1, v_2 \in g, \quad g \in \mathcal{G}, \quad v_1, v_2 \in \mathcal{V}^b
\end{aligned} \tag{34}$$

To generate demand scenarios that satisfy constraints (32) and (33), we use the method proposed in [39]. Its original purpose was to generate samples from the Dirichlet distribution, but it can be used for a special case of the Dirichlet distribution that is equivalent to a uniform distribution over a simplex in 3-dimensions. Such a simplex is exactly described by (32) and (33) for each time step. Hence we can apply it for all time-steps and reject all samples that do not satisfy constraints (34). Note that this method is insufficient for network stations with more than three boundary nodes.

In addition to flow demands, we require a pressure forecast for all boundary nodes. Our only requirements here is that the pressures between adjacent time steps for a single node not fluctuate heavily and that the bounds are respected. We create a bound on the range of pressure values by finding maximum and minimum values over all nodes and time steps in our test set. We once again assume our samples to be uniformly distributed and sample appropriately over (35) with rejection of samples that do not respect constraint (36). Note that many scenarios generated by this approach are unlikely to happen in practice, as the pressure and flow profiles may not match.

$$\begin{aligned}
M_p^+ &= \max_{v \in \mathcal{V}^b, t \in \mathcal{T}} \hat{p}_{v,t} & M_p^- &= \min_{v \in \mathcal{V}^b, t \in \mathcal{T}} \hat{p}_{v,t} \\
\hat{p}_{v,t} &\in [M_p^- - 0.05(M_p^+ - M_p^-), M_p^+ + 0.05(M_p^+ - M_p^-)]
\end{aligned} \tag{35}$$

$$|\hat{p}_{v,t} - \hat{p}_{v,t-1}| \leq 5 \quad \forall t \in \mathcal{T}, \quad v \in \mathcal{V}^b \quad (36)$$

Combining the two procedures from above yields the artificial forecast data generation method described in Algorithm 1.

Algorithm 1: Boundary Value Forecast Generator

Result: A forecast of pressure and flow values over the time horizon
flow_forecast = Sample simplex (32)(33) uniformly, rejecting via (34) ;
pressure_forecast = Sample (35) uniformly, rejecting via (36) ;
return (flow_forecast, pressure_forecast)

5.1.2 Operation Mode Sequence Generation

During offline training, \mathbb{D}_{θ_2} requires optimal solutions for a fixed z_1 . In Algorithm 2 we outline a naive yet effective approach of generating reasonable z_1 values, i.e., operation mode sequences:

Algorithm 2: Operation Mode Sequence Generator

Result: An Operation Mode per time step
operation_modes = [] ;
for $t = 1$; $t < |\mathcal{T}|$; $t = t + 1$ **do**
 if $t == 1$ **then**
 | new_operation_mode = rand(\mathcal{O}) ;
 else if $\text{rand}(0,1) \geq 0.9$ **then**
 | new_operation_mode = rand($\mathcal{O} \setminus \text{new_operation_mode}$) ;
 end
 operation_modes.append(new_operation_mode) ;
end
return operation_modes

5.1.3 Initial State Generation

Many coefficients of A_π are invariant due to static network topology. Many others however are found by substituting multiple parameters into an equation describing gas properties. This information is contained in the initial state, and we generate them similar to boundary forecasts:

$$c_{\text{state}} \in \{\text{Temperature, Inflow Norm Density, Molar Mass, Pseudo Critical Temperature, Pseudo Critical Pressure}\} \quad (37)$$

$$M_c^+ = \max_{\text{state} \in \text{initial states}} c_{\text{state}} \quad M_c^- = \min_{\text{state} \in \text{initial states}} c_{\text{state}} \quad (38)$$

$$c_{\text{state}} \in [M_c^- - 0.05(M_c^+ - M_c^-), M_c^+ + 0.05(M_c^+ - M_c^-)]$$

We now have the tools to generate synthetic initial states, see Algorithm 3.

Algorithm 3 is designed to output varied and valid initial states w.r.t our MILP formulation. However, it comes with some drawbacks. Firstly, the underlying distribution of demand scenarios for both flow and pressure are probably not uniform nor conditionally independent. Moreover, the sampling range we use is significantly larger than that of our test set as we take single maximum and minimum values over all nodes. Secondly, the choice of operation modes that occur in reality is also not uniform. In reality, some operation modes occur with a much greater frequency than others. Our data is thus more dynamic than reality, and likely to contain operation mode choices that do match the demand scenarios. Finally, we rely on a MILP solver to generate new initial states in our final step. Hence we cannot rule out the possibility of a slight bias. One example would be the case of a repeated scenario, which has multiple

optimal solutions, but the MILP solver always returns an identical solution.

Algorithm 3: Initial State Generator

Input: Desired time-step distance $j \in [1, \dots, k]$
Result: An initial state to the transient gas optimisation problem
flow_forecast, pressure_forecast = Boundary Prognosis Generator() ^a ;
gas_constants = Sample (38) uniformly ;
initial_state = Select random state from real-world data ;
 $\pi = (\text{flow_forecast}, \text{pressure_forecast}, \text{gas_constants}, \text{initial_state})$ ^b ;
 $z_1 = \text{Operation Mode Sequence Generator}()$ ^c ;
 $\mathbb{P}_\pi^{z_1} = \text{generate from } \pi \text{ and } z_1$;
(state_1, \dots , state_k) = Optimal solution states from solving $\mathbb{P}_\pi^{z_1}$;
return state_j

^aSee Algorithm 1

^bNote that in general our π does not include gas_constants. This is because the information is generally encoded in initial_state. Our gas_constants in this context are randomly generated however, and may not match the initial_state. This does not affect solving as these values are simply taken as truths.

^cSee Algorithm 2

Algorithm 4: Synthetic Gas Data Generator

Input: num_states, num_scenarios, time_step_difference
Result: num_scenarios many gas instances and their optimal solutions
initial_states = [] ;
for $i = 0$; $i < \text{num_states}$; $i = i + 1$ **do**
| initial_states.append(Initial State Generator(time_step_difference))^a ;
end
forecasts = [] ;
for $i = 0$; $i < \text{num_scenarios}$; $i = i + 1$ **do**
| flow_forecast, pressure_forecast = Boundary Prognosis Generator()^b ;
| forecasts.append((flow_forecast, pressure_forecast)) ;
end
solve_data = [] ;
for $i = 0$; $i < \text{num_scenarios}$; $i = i + 1$ **do**
| $z_1 = \text{Operation Mode Sequence Generator}()$ ^c ;
| initial_state = Uniformly select from initial_states ;
| $\pi = (\text{forecasts}[i], \text{initial_state})$;
| $\mathbb{P}_\pi^{z_1} = \text{Create MILP from } \pi \text{ and } z_1$;
| solution = Solve $\mathbb{P}_\pi^{z_1}$;
| solve_data.append(($z_1, \pi, \text{solution}$)) ;
end
return solve_data

^aSee Algorithm 3

^bSee Algorithm 1

^cSee Algorithm 2

In the case of initial state generation, we believe that further research needs to be performed. Our method is effective in the context of machine learning where we aim for a diverse set of data, but it is naive and incapable of ensuring that generated boundary scenarios are realistic.

5.1.4 Complete Transient Gas Instance Generation

To train \mathbb{D}_{θ_2} and \mathbb{G}_{θ_1} , we need both the transient gas transportation scenario, and an optimal solution for it. Combining the generation methods for synthetic data in subsections 5.1.1, 5.1.2, 5.1.3, and the solving process of the created instances, we derive Algorithm 4.

5.2 Experimental Design

We generated our initial training and validation sets offline. To do so we use Algorithm 4 with inputs: `num_states` = 10^4 , `num_scenarios` = 4×10^6 , and `time_step_difference` = 8. This initial training data is exclusively used for training \mathbb{D}_{θ_2} , and is split into a training set of size 3.2×10^6 , a test set of 4×10^5 , and a validation set of 4×10^5 .

The test set is checked against at every epoch, while the validation set is only referred to at the end of the initial training. Following this initial training, we begin to train $\mathbb{N}_{\{\theta_1, \theta_2\}}$ as a whole, alternating between \mathbb{G}_{θ_1} and \mathbb{D}_{θ_2} . The exact algorithm is given in 5, which references functions provided in Appendix A. For training, we used the Adam algorithm [27] as our descent method. The associated parameters to this algorithm and a complete set of other training parameters are listed in Table 4. In the case of a parameter being non-listed, the default value was used. The intention behind our training method is to ensure that $\mathbb{N}_{\{\theta_1, \theta_2\}}$ receives no real-world data prior to its final evaluation. With this method we hope to show that synthetic data is sufficient for training purposes and that $\mathbb{N}_{\{\theta_1, \theta_2\}}$ successfully generalises to additional data sets. However, we should note that Algorithm 3 does use real-world data as a starting point from which to generate artificial data.

Algorithm 5: Neural Network Training

```
Input: Neural network  $\mathbb{N}_{\{\theta_1, \theta_2\}}$ , prelabelled_data  
Result: Trained neural network  $\mathbb{N}_{\{\theta_1, \theta_2\}}$   
set_trainable( $\mathbb{D}_{\theta_2}$ );  
set_untrainable( $\mathbb{G}_{\theta_1}$ );  
Discriminator Pretraining( $\mathbb{D}_{\theta_2}$ , prelabelled_data) a ;  
softmax_temperature = 0;  
data = [];  
for  $i = 0$ ;  $i < num\_epochs$  do  
    set_trainable( $\mathbb{G}_{\theta_1}$ );  
    set_untrainable( $\mathbb{D}_{\theta_2}$ );  
    for  $i = 0$ ;  $i < num\_generator\_epochs$  do  
        softmax_temperature += 1;  
        set( $\mathbb{G}_{\theta_1}$ , softmax_temperature);  
        loss = Generator Training( $\mathbb{N}_{\{\theta_1, \theta_2\}}$ ) b ;  
        if  $loss \leq stopping\_loss\_generator$  then  
            | break;  
        end  
    end  
    set_trainable( $\mathbb{D}_{\theta_2}$ );  
    set_untrainable( $\mathbb{G}_{\theta_1}$ );  
    data = Prepare Discriminator Training Data( $\mathbb{N}_{\{\theta_1, \theta_2\}}$ , data) c ;  
    mixed_data = MixData(data, prelabelled_data, num_prelabelled);  
    training_data, test_data = split_data(mixed_data, ratio_test);  
    optimizer = Adam(learning_rate, weight_decay) d ;  
    lr_scheduler = ReduceLRonPlateau e (patience, factor);  
    dataloader = DataLoader(training_data, batch_size, shuffle=True);  
    for  $i = 0$ ;  $i < num\_discriminator\_epochs$  do  
        Discriminator Training Loop( $\mathbb{D}_{\theta_2}$ , dataloader, optimizer) f ;  
        lr_scheduler.step();  
        test_loss = compute_L1Loss( $\mathbb{D}_{\theta_2}$ , test_data);  
        if  $test\_loss \leq stopping\_loss\_discriminator$  then  
            | break;  
        end  
    end  
end  
return  $\mathbb{N}_{\{\theta_1, \theta_2\}}$ 
```

^aSee Algorithm 9

^bSee Algorithm 11

^cSee Algorithm 8

^dSee [27] pytorch.org/docs/stable/optim.html?highlight=adam#torch.optim.Adam.

^eSee pytorch.org/docs/stable/optim.html#torch.optim.lr_scheduler.ReduceLRonPlateau.

^fSee Algorithm 10

We consider the solution of $\mathbb{P}_{\pi}^{\hat{z}_1}$ as a primal heuristic for the original problem

\mathbb{P}_π . Due to our usage of slack, i.e. the application of variables x_2 , any valid solution for $\mathbb{P}_\pi^{z_1}$ is a valid solution of \mathbb{P}_π . We aim to incorporate $\mathbb{N}_{\{\theta_1, \theta_2\}}$ in a global MIP context and do this by using a partial solution of $\mathbb{P}_\pi^{z_1}$ as a warm-start suggestion for \mathbb{P}_π . The partial solution consists of \hat{z}_1 , an additional set of binary variables called the flow directions, which are a subset of z_2 in (1), and $p_{v,t} \forall v \in \mathcal{V}^b, t \in \mathcal{T}$, which are a subset of x_1 in (1). Note that partial solutions are used as instances are numerically difficult. In doing so, we hope to generate valid solutions quickly, and speed up the global solution process. The primal heuristic and warm-start algorithm can be seen in Algorithms 6 and 7 respectively.

Algorithm 6: Primal Heuristic

Input: \mathbb{P}_π
 $\hat{z}_1 = \mathbb{G}_{\theta_1}(\pi)$;
 $\mathbb{P}_\pi^{\hat{z}_1} = \text{Create MILP from } \pi \text{ and } \hat{z}_1$;
solution = Solve $\mathbb{P}_\pi^{\hat{z}_1}$;
return solution ;
Result: Optimal solution of $\mathbb{P}_\pi^{\hat{z}_1}$, primal solution of \mathbb{P}_π .

Algorithm 7: Warm Start Algorithm

Input: \mathbb{P}_π
primal_solution = Primal Heuristic(\mathbb{P}_π)^a ;
optimum = Solve \mathbb{P}_π with primal_solution as a warm-start suggestion ;
Result: Optimal solution of \mathbb{P}_π

^aSee Algorithm 6

For our experiments we used PyTorch 1.4.0 [34] as our ML modelling framework, Pyomo v5.5.1 [21, 22] as our MILP modelling framework, and Gurobi v9.02 [19] as our MILP solver. The MILP solver settings are available in Table 5 in Appendix A. $\mathbb{N}_{\{\theta_1, \theta_2\}}$ was trained on a machine running Ubuntu 18, with 384 GB of RAM, composed of 2x *Intel(R) Xeon(R) Gold 6132* running @ 2.60GHz, and 4x *NVIDIA Tesla V100 GPU-NVTV100-16*. The final evaluation times were performed on a cluster using 4 cores and 16 GB of RAM of a machine composed of 2x *Intel Xeon CPU E5-2680* running @ 2.70 GHz.

Our validation set for the final evaluation of $\mathbb{N}_{\{\theta_1, \theta_2\}}$ consists of 15 weeks of live real-world data from our project partner OGE. Instances are on average 15 minutes apart for this period and total 9291.

All instances, both in training and test, contain 12 time steps (excluding the initial state) with 30 minutes between each step. Additionally, we focus on Station D from [24], and present only results for this station. The statistics for Station D can be seen in Table 1, and its topology in Figure 4. Station D can be thought of as a T intersection, and is of average complexity compared to the

stations presented in [24]. The station contains 6 boundary nodes, but they are paired, such that for each pair only one can be active, i.e., have non-zero flow. Due to this, our sampling method in subsection 5.1.1 exists in 3-dimensions and is uniform $\forall t \in \mathcal{T}$.

Name	$ \mathcal{V} $	$ \mathcal{A} $	$\frac{\sum_{a \in \mathcal{A}^{bi}} L_a}{ \mathcal{A}^{pi} }$	$ \mathcal{C}_a \forall a \in \mathcal{A}^{cs}$	$ \mathcal{O} $	$ \mathcal{V}^b $	$ \mathcal{A}^{va} $
D	31	37	0.404 km	2, 6	56	3x2	11

Table 1: Overview of different properties of station D.

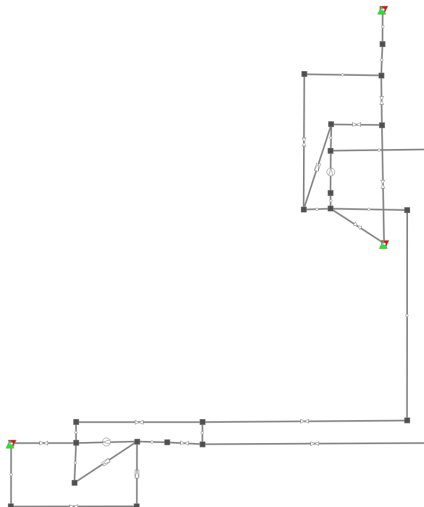


Figure 4: Topology of Station D.

5.3 Exact Network Designs

As a large portion of our input data into both \mathbb{G}_{θ_1} and \mathbb{D}_{θ_2} is time-expanded data, we originally believed that the ideal design would be a series of LSTMs [25]. Preliminary results however showed that convolutional neural networks (CNNs) were more effective for our problem, in particular when using Inception Blocks, see [42].

The exact block design used in $\mathbb{N}_{\{\theta_1, \theta_2\}}$ can be seen in Figure 3, and the general layout in Figure 1. For the complete network design we refer readers to Figure 14 and Table 6 in the Appendix.

6 Computational Results

We partition our results into three subsections. The first focuses on the training results of $\mathbb{N}_{\{\theta_1, \theta_2\}}$, the second on our data generation methods, while the third is concerned with our results on the 15 weeks of real-world transient gas data. Note that when training we scaled $f(\mathbb{P}_\pi^{z_1})$ values by 500 to reduce the magnitude of the losses. For visualisation purposes of comparing the performance of $\mathbb{N}_{\{\theta_1, \theta_2\}}$ and our data generation methods, we re-scaled all results.

6.1 Training Results



Figure 5: The loss per epoch of \mathbb{D}_{θ_2} during the initial training of Algorithm 9. The dashed lines show the performance of \mathbb{D}_{θ_2} after $\mathbb{N}_{\{\theta_1, \theta_2\}}$ has been completely trained.

Figure 5 shows the training loss throughout the initial offline training. We see that \mathbb{D}_{θ_2} learns how to accurately predict $f(\mathbb{P}_\pi^{z_1})$ as the loss decreases. This is a required result, as without a trained discriminator we cannot expect to train a generator. Both the training and test loss converge to approximately 1000, which is excellent considering the generated $f(\mathbb{P}_\pi^{z_1})$ range well into the millions. As visible by both the test loss and final validation loss, we see \mathbb{D}_{θ_2} generalises to $\mathbb{P}_\pi^{z_1}$ instances of our validation set that it has not seen. This generalisation ability doesn't translate perfectly to real-world data however. This is due to the underlying distribution of real-world data and our generated data being substantially different. Despite this we believe that an L1 loss, in this case simply the average distance between $\hat{f}(\mathbb{P}_\pi^{z_1})$ and $f(\mathbb{P}_\pi^{z_1})$, of 10000 is still very good. We discuss the issues of different distributions in subsection 6.2.



Figure 6: The loss per epoch of \mathbb{D}_{θ_2} as it is trained using Algorithm 5

The loss during training using Algorithm 5 for \mathbb{D}_{θ_2} is shown in Figure 6, and for \mathbb{G}_{θ_1} in Figure 7. The cyclical nature of the \mathbb{D}_{θ_2} loss is caused by the re-training of \mathbb{G}_{θ_1} , which learns how to induce sub-optimal predictions from the then static \mathbb{D}_{θ_2} . These sub-optimal predictions are quickly re-learned, but highlight that learning how to perfectly predict $f(\mathbb{P}_{\pi}^{\hat{z}_1})$ over all possibilities, potentially due to the rounded nature of \hat{z}_1 , is unlikely without some error. Figure 7 (left) shows the loss over time of \mathbb{G}_{θ_1} as it is trained, with Figure 7 (right) displaying magnified losses for the final epochs. We observe that \mathbb{G}_{θ_1} quickly learns important z_1 decision values. We hypothesise that this quick descent is helped by \hat{z}_1 that are unlikely given our generation method in Algorithm 2. The loss increases following this initial decrease in the case of \mathbb{G}_{θ_1} , showing the ability of \mathbb{D}_{θ_2} to further improve. It should also be noted that significant step-like decreases in loss are absent in both (left) and (right) of Figure 7. Such steps would indicate \mathbb{G}_{θ_1} discovering new important z_1 values (operation modes). The diversity of produced operation modes however, see Figure 12, implies that early in training a complete spanning set of operation modes is derived, and the usage of their ratios is then learned and improved.

6.2 Data Generation Results

As an interlude between results from $\mathbb{N}_{\{\theta_1, \theta_2\}}$, we outline the performance of our synthetic gas network data generation methods. Figure 8 (left) shows how our generated flow prognosis compares to that of historic real-world data. We see that Nodes A, B, and C are not technically entry or exits, but over historical data are dominated by a single orientation for each node. Specifically, Node C is the general entry, and Nodes A / B are the exits. In addition to the general orientation, we see that each node has significantly different ranges and distributions. These observations highlight the simplicity of our data generation methods, as we see near identical distributions for all nodes over the artificial

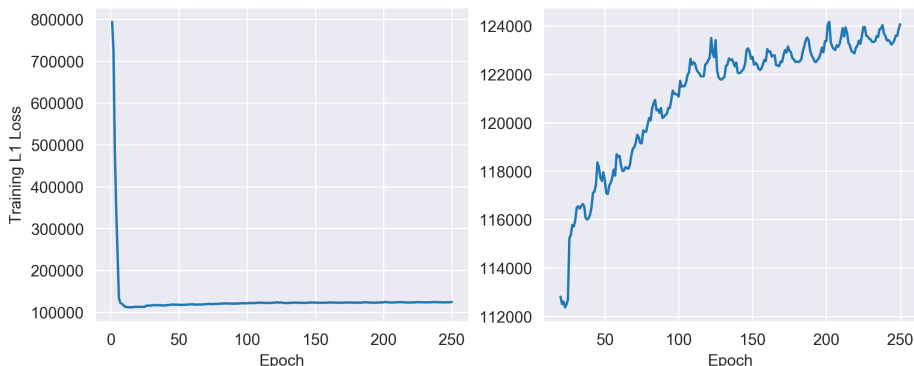


Figure 7: (Left) The loss per epoch of \mathbb{G}_{θ_1} as it is trained using Algorithm 5. On the left the loss over all epochs is shown. (Right) A magnified view of the loss starting from epoch 20.

data. We believe this calls for further research in prognosis generation methods. Figure 8 (right) shows our pressure prognosis compared to that of historic values. Unlike historic flow values, we observe little difference between historic pressure values of different nodes. This is supported by the optimal choices z_1^* over the historic data, see Figure 12, as in a large amount of cases compression is not needed and the network station is in bypass. Note that each corresponding entry (+) and exit (-) have identical pressure distributions due to the way they are constructed.

A further comparison of how our generated data compares to historic data can be seen in Figure 9. Here one can see the distribution of $\hat{f}(\mathbb{P}_\pi^{\hat{z}_1})$ and $f(\mathbb{P}_\pi^{\hat{z}_1})$ for the generated validation set, and $\hat{f}(\mathbb{P}_\pi^{\hat{z}_1})$ and $f(\mathbb{P}_\pi)$ for the real-world data. As expected, the distributions are different depending on whether the data is artificial or not. Our data generation was intended to be simplistic, and as independent as possible from the historic data. As such, the average scenario has optimal solution larger than that of any real-world data point. The performance of \mathbb{D}_{θ_2} is again clearly visible here, with $\hat{f}(\mathbb{P}_\pi^{\hat{z}_1})$ and $f(\mathbb{P}_\pi^{\hat{z}_1})$ being near identical over the artificial data, keeping in mind that these data points were never used in training. We see that this ability to generalise is relatively much worse on real-world data, mainly due to the the lower values of $f(\mathbb{P}_\pi)$ over this data. Figure 9 (right) shows the results with log-scale axes to better highlight this disparity. It should be noted that the real-world instances with larger $f(\mathbb{P}_\pi)$ are predicted quite well, and all real-world instances have an L1 distance between $\hat{f}(\mathbb{P}_\pi^{\hat{z}_1})$ and $f(\mathbb{P}_\pi)$ that is small in terms of absolute differences.

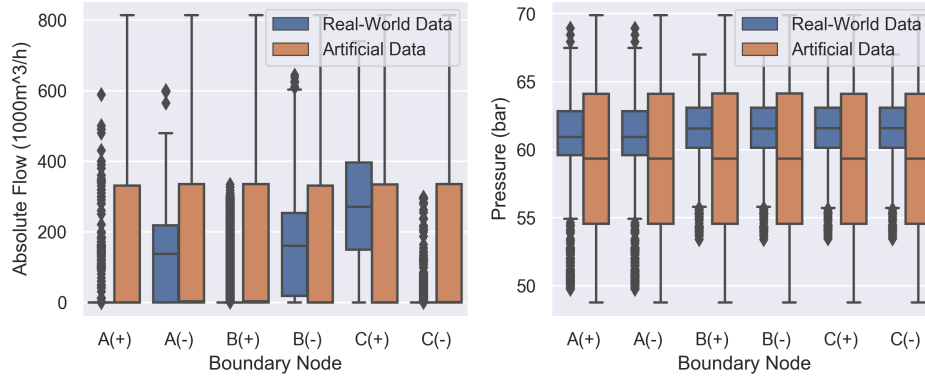


Figure 8: Comparison of generated flow (Left) / pressure (Right) value distributions per node vs. the distribution seen in real-world data.

6.3 Real-World Results

We now present results of our fully trained $\mathbb{N}_{\{\theta_1, \theta_2\}}$ applied to the 15 weeks of real-world data. Note that we had to remove 651 instances from our 9291 instances, as the warm-start resulted in an optimal solution value further away than the optimality tolerances we set. These instances have been kept in the graphics, but are marked and conclusions will not be drawn from them. We believe the problems with reproducibility are caused by the numeric difficulties in managing the pipe equality constraints.

Figure 10 shows the comparison of $f(\mathbb{P}_\pi^{\hat{z}_1})$ and $f(\mathbb{P}_\pi)$. In a similar manner to \mathbb{D}_{θ_2} , we see that \mathbb{G}_{θ_1} struggles with instances where $f(\mathbb{P}_\pi)$ is small. This is visible in the bottom left, where we see $f(\mathbb{P}_\pi^{\hat{z}_1})$ values much larger than $f(\mathbb{P}_\pi)$ for like π . This comes as little surprise given the struggle of \mathbb{D}_{θ_2} with small $f(\mathbb{P}_\pi)$ values. Drawing conclusions becomes more complicated for instances with larger $f(\mathbb{P}_\pi)$ values, because the majority hit the time limit. We can clearly see however, the value of our primal heuristic. There are many cases, those below the line $f(\mathbb{P}_\pi^{\hat{z}_1}) = f(\mathbb{P}_\pi)$, where our primal heuristic retrieves a better solution than the MILP solver does in one hour. Additionally, we see that no unsolved point above the line is very far from the line, showing that our primal heuristic produced a comparable, sometimes equivalent solution in a much shorter time frame. For a comparison of solve-times, see Table 2.

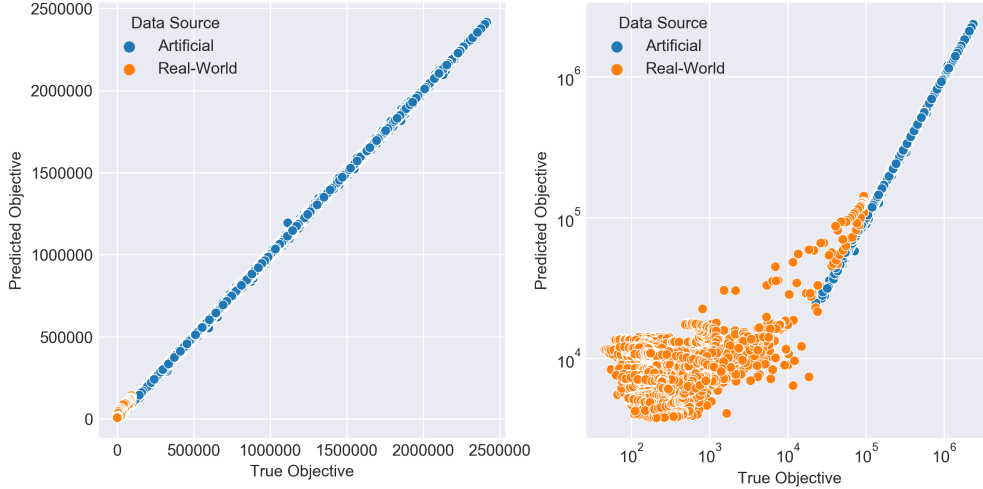


Figure 9: $\hat{f}(\mathbb{P}_\pi^{\hat{z}_1})$ for the validation set, and $\hat{f}(\mathbb{P}_\pi^{\hat{z}_1^*})$ for real-world data, compared to $f(\mathbb{P}_\pi^{\hat{z}_1})$ and $f(\mathbb{P}_\pi)$ respectively. Linear scale (Left) and log-scale (Right).

	Mean	Median	STD	Min	Max
$\mathbb{N}_{\{\theta_1, \theta_2\}}$ Inference Time (s)	0.009	0.008	0.001	0.008	0.017
Warmstarted \mathbb{P}_π Time (s)	100.830	9.380	421.084	0.130	3600.770
\mathbb{P}_π Time (s)	147.893	24.380	463.279	3.600	3601.280
$\mathbb{P}_\pi^{\hat{z}_1}$ + Warmstarted \mathbb{P}_π Time (s)	103.329	12.130	424.543	0.190	3726.110
$\mathbb{P}_\pi^{\hat{z}_1}$ Time (s)	2.499	1.380	12.714	0.060	889.380

Table 2: Solve time statistics for different solving strategies.

Figure 11 shows the performance of the predictions $\hat{f}(\mathbb{P}_\pi^{\hat{z}_1})$ compared to $f(\mathbb{P}_\pi^{\hat{z}_1})$. Interestingly, \mathbb{D}_{θ_2} generally predicts $\hat{f}(\mathbb{P}_\pi^{\hat{z}_1})$ values slightly larger than $f(\mathbb{P}_\pi^{\hat{z}_1})$. We expect this for the smaller valued instances, as we know that \mathbb{D}_{θ_2} struggles with $f(\mathbb{P}_\pi^{\hat{z}_1})$ instances near 0, but the trend is evident for larger valued instance too. The closeness of the data points to the line $\hat{f}(\mathbb{P}_\pi^{\hat{z}_1}) = f(\mathbb{P}_\pi^{\hat{z}_1})$ show that \mathbb{D}_{θ_2} can adequately predict \hat{z}_1 solutions from \mathbb{G}_{θ_1} despite the change in data sets. Figure 10 showed that \mathbb{G}_{θ_1} successfully generalised to a new data set, albeit with difficulties around instances with $f(\mathbb{P}_\pi)$ valued near 0. From Figures 10 and 11, we can see that the entire $\mathbb{N}_{\{\theta_1, \theta_2\}}$ generalises to unseen real-world instances, despite some generalisation loss.

We now compare the operation modes \hat{z}_1 , which are generated by \mathbb{G}_{θ_1} , and the z_1^* , which are produced by our MILP solver. To do so we use the following naming convention: We name the three pairs of boundary nodes N (north), S (south), and W (west). Using W_NS_C.2 as an example, we know that flow comes from W, and goes to N and S. The C in the name stands for active

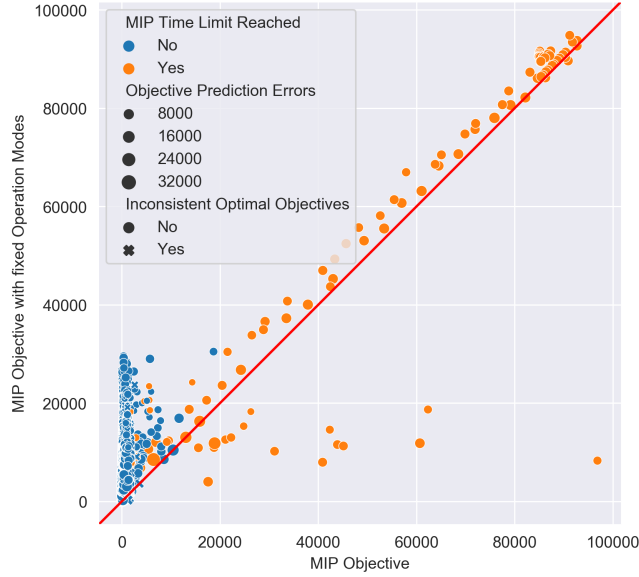


Figure 10: A comparison of $f(\mathbb{P}_\pi^{\hat{z}_1})$ and $f(\mathbb{P}_\pi)$ for all real-world data instances.

	<i>NW_NS_1</i>	<i>NS_SW_2</i>	<i>N_SW_C_1</i>	<i>NS_NS_W_1</i>	<i>W_NS_C_1</i>	<i>NS_SW_1</i>	<i>NW_S_2</i>	<i>NS_SW_3</i>	<i>W_NS_C_2</i>	<i>NW_S_1</i>	<i>Other</i>
<i>NW_NS_1</i>	884	22	0	9529	31	37	2436	4	24	397	82
<i>NS_SW_2</i>	48	102	1	40298	0	114	630	24	0	51	13
<i>N_SW_C_1</i>	0	27	65	11008	0	4	0	2	0	0	55
<i>NS_NS_W_1</i>	41	29	0	26509	0	28	557	9	0	49	15
<i>W_NS_C_1</i>	0	0	0	0	0	0	0	0	0	0	0
<i>NS_SW_1</i>	0	0	0	76	0	1	0	0	0	0	0
<i>NW_S_2</i>	4	0	0	0	0	0	2	0	0	1	1
<i>NS_SW_3</i>	6	7	0	5220	0	7	108	1	0	4	5
<i>W_NS_C_2</i>	28	0	0	0	136	0	0	0	93	0	0
<i>NW_S_1</i>	30	11	0	2880	0	12	315	2	0	30	6
<i>Other</i>	0	1	0	78	0	0	0	0	0	0	1

Table 3: Operation Mode Correlation Matrix between \hat{z}_1 and z_1^* .

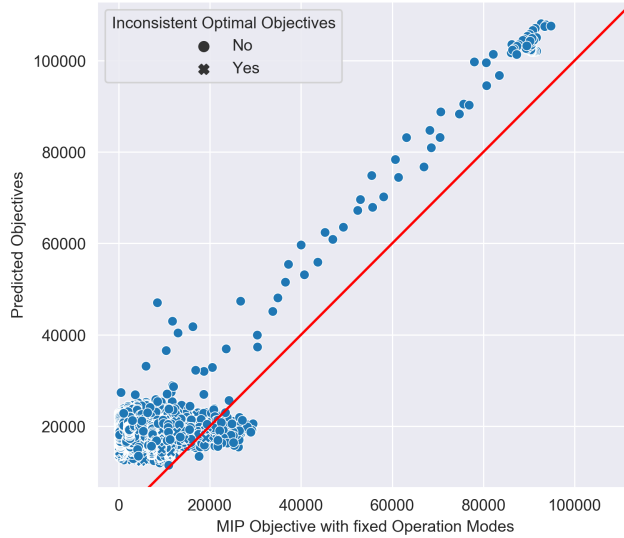


Figure 11: A comparison of $\hat{f}(\mathbb{P}_\pi^{z_1^*})$ and $f(\mathbb{P}_\pi^{z_1^*})$ for all real-world data instances.

compression, and the final index is to differentiate between duplicate names. As seen in Figure 12, which plots the frequency of specific z_1 if they occurred more than 50 times, a single choice dominates z_1^* . This is interesting, because we expected there to be a lot of symmetry between z_1 , with the MILP solver selecting symmetric solutions with equal probability. For instance, take W_NS_C_1 and take W_NS_C_2. $\mathbb{N}_{\{\theta_1, \theta_2\}}$ only ever predicts W_NS_C_2, however with half the frequency the MILP solver selects each of them. This indicates that from the MILP’s point of view they are symmetric, and either can be chosen, while $\mathbb{N}_{\{\theta_1, \theta_2\}}$ has recognised this and converged to a single choice. We can support this by analysing the data, where the difference in W_NS_C_1 and W_NS_C_2 is which compressor machine is used, with both machines being identical. This duplicate choice apparently does not exist in bypass modes however, where the uniqueness of z_1 , determined by valve states, results in different $f(\mathbb{P}_\pi^{z_1^*})$ values. It is observable then that for the majority of instances NS_NSW_1 is the optimal choice, and that $\mathbb{N}_{\{\theta_1, \theta_2\}}$ has failed to identify its central importance. We believe this is due to the training method, where over generalisation to a single choice is strongly punished. For a comprehensive overview of the selection of operation modes and the correlation between \hat{z}_1 and z_1^* , we refer interested readers to Table 3.

As discussed above, $\mathbb{N}_{\{\theta_1, \theta_2\}}$ cannot reliably produce z_1^* . Nevertheless, it produces near-optimal \hat{z}_1 suggestions, which are still useful in a warm-start context, see Algorithm 7. The results of our warm-start algorithm are displayed in Figure 13. Our warm-start suggestion was successful 72% of the time, and the algorithm resulted in an average speed up of 60.5%. We use the shifted geomet-

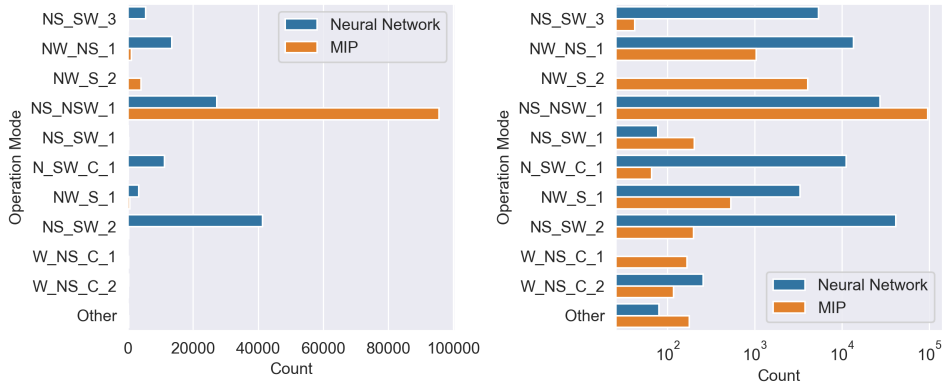


Figure 12: Frequency of operation mode choice by \mathbb{G}_{θ_1} compared to MILP solver for all real-world instances. (Left) Linear scale, and (Right) log scale.

ric mean with a shift of 1 for this measurement to avoid distortion by relative variations of the smaller valued instances. Especially surprising is that some instances that were previously unsolvable within the time-limit were easily solvable given the warm-start suggestion. In addition, many of the solvable but complicated instances are also solved near instantly with the warm-start suggestion. As such, we have created an effective primal heuristic that is both quick to run and beneficial in the context of locating a globally optimal solution.

7 Conclusion

In this paper, we presented a dual neural network design for generating decisions in a MILP. This design is trained without ever solving the MILP with unfixed decision variables. The neural network is both used as a primal heuristic and used to warm-start the MILP solver for the original problem. We proved the usefulness of our design on the transient gas transportation problem. While doing so we created methods for generating synthetic transient gas data for training purposes, reserving an unseen 9291 real-world instances for validation purposes. Despite some generalisation loss, our trained neural network results in a primal heuristic that takes on average 2.5s to run, and results in a 60.5% decrease in global optimal solution time when used in a warm-start context.

While our approach is an important step forward in neural network design and ML’s application to gas transport, we believe that there exists four primary directions for future research. The first of which is to convert our approach into more traditional reinforcement learning, and then utilise policy gradient approaches, see [44]. The major hurdle to this approach is that much of the computation would be shifted online, requiring many more calls to solve the induced MILPs. This could be offset however, by using our technique to ini-

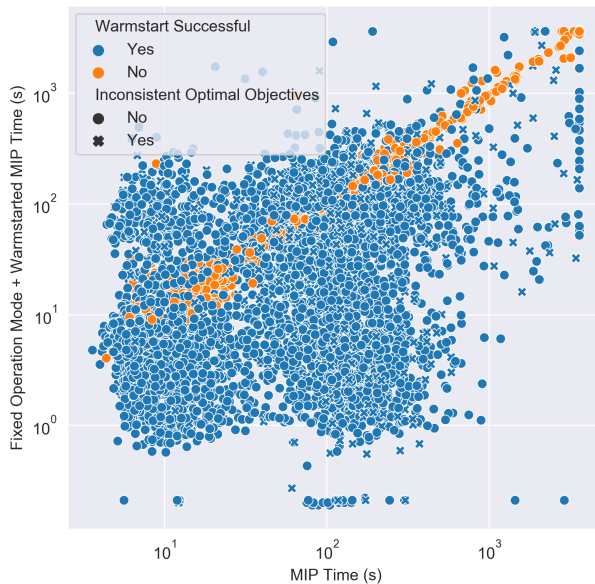


Figure 13: The combined running time of solving $\mathbb{P}_\pi^{\hat{z}_1}$, and solving a warm-started \mathbb{P}_π , compared to solving \mathbb{P}_π directly.

tialise the weights for such an approach, thereby avoiding early stage training difficulties with policy gradient approaches. The second is focused on the recent improvements in Graph Neural Networks, see [16]. Their ability to generalise to different input sizes would permit the creation of a single NN over multiple network stations or gas network topologies. Thirdly, there exists a large gap in the literature w.r.t data generation for transient gas networks. Improved methods are needed, which are scalable and result in real-world like data. Finally, although we focused on the transient gas transportation problem, our approach can be generalised to arbitrary problem classes.

Acknowledgements

The work for this article has been conducted in the Research Campus MODAL funded by the German Federal Ministry of Education and Research (BMBF) (fund numbers 05M14ZAM, 05M20ZBM), and was supported by the German Federal Ministry of Economic Affairs and Energy (BMWi) through the project UNSEEN (fund no 03EI1004D).

References

- [1] T. Achterberg. *Constraint integer programming*. PhD thesis, Technische Universität Berlin, 2007.
- [2] E. Balas. The Convex Hull of a Disjunctive Set. In *Disjunctive Programming*, pages 17–39. Springer International Publishing, Cham, 2018.
- [3] R. Baltean-Lugojan, P. Bonami, R. Misener, and A. Tramontani. Scoring positive semidefinite cutting planes for quadratic optimization via trained neural networks. *optimization-online preprint 2018/11/6943*, 2019.
- [4] J. Beliën, E. Demeulemeester, and B. Cardoen. A decision support system for cyclic master surgery scheduling with multiple objectives. *Journal of scheduling*, 12(2):147, 2009.
- [5] Y. Bengio, A. Lodi, and A. Prouvost. Machine learning for combinatorial optimization: a methodological tour d’horizon. *arXiv preprint arXiv:1811.06128*, 2018.
- [6] D. Bertsimas and B. Stellato. The voice of optimization. *arXiv preprint arXiv:1812.09991*, 2018.
- [7] D. Bertsimas and B. Stellato. Online mixed-integer optimization in milliseconds. *arXiv preprint arXiv:1907.02206*, 2019.
- [8] R. Burlacu, H. Egger, M. Groß, A. Martin, M. E. Pfetsch, L. Schewe, M. Sirvent, and M. Skutella. Maximizing the storage capacity of gas networks: a global minlp approach. *Optimization and Engineering*, 20(2):543–573, 2019.
- [9] Z. Chen, Y. Zhong, X. Ge, and Y. Ma. An actor-critic-based uav-bss deployment method for dynamic environments. *arXiv preprint arXiv:2002.00831*, 2020.
- [10] S. Dempe. *Foundations of bilevel programming*. Springer Science & Business Media, 2002.
- [11] J.-Y. Ding, C. Zhang, L. Shen, S. Li, B. Wang, Y. Xu, and L. Song. Optimal solution predictions for mixed integer programs. *arXiv preprint arXiv:1906.09575*, 2019.
- [12] M. Etheve, Z. Alès, C. Bissuel, O. Juan, and S. Kedad-Sidhoum. Reinforcement learning for variable selection in a branch and bound algorithm. *arXiv preprint arXiv:2005.10026*, 2020.
- [13] J. Fang, Q. Zeng, X. Ai, Z. Chen, and J. Wen. Dynamic optimal energy flow in the integrated natural gas and electrical power systems. *IEEE Transactions on Sustainable Energy*, 9(1):188–198, 2017.
- [14] A. Ferber, B. Wilder, B. Dilina, and M. Tambe. Mipaal: Mixed integer program as a layer. *arXiv preprint arXiv:1907.05912*, 2019.

- [15] M. Fischetti and A. Lodi. Local branching. *Mathematical programming*, 98(1-3):23–47, 2003.
- [16] M. Gasse, D. Chételat, N. Ferroni, L. Charlin, and A. Lodi. Exact combinatorial optimization with graph convolutional neural networks. In *Advances in Neural Information Processing Systems*, pages 15554–15566, 2019.
- [17] I. Goodfellow. Nips 2016 tutorial: Generative adversarial networks. *arXiv preprint arXiv:1701.00160*, 2016.
- [18] I. Goodfellow, Y. Bengio, and A. Courville. *Deep learning*. MIT press, 2016.
- [19] L. Gurobi Optimization. Gurobi optimizer reference manual, 2020.
- [20] H. Hanachi, C. Mechefske, J. Liu, A. Banerjee, and Y. Chen. Performance-based gas turbine health monitoring, diagnostics, and prognostics: A survey. *IEEE Transactions on Reliability*, 67(3):1340–1363, 2018.
- [21] W. E. Hart, C. D. Laird, J.-P. Watson, D. L. Woodruff, G. A. Hackebeil, B. L. Nicholson, and J. D. Siirola. *Pyomo—optimization modeling in python*, volume 67. Springer Science & Business Media, second edition, 2017.
- [22] W. E. Hart, J.-P. Watson, and D. L. Woodruff. Pyomo: modeling and solving mathematical programs in python. *Mathematical Programming Computation*, 3(3):219–260, 2011.
- [23] F. Hennings. Benefits and limitations of simplified transient gas flow formulations. In *Operations Research Proceedings 2017*, pages 231–237. Springer, 2018.
- [24] F. Hennings, L. Anderson, K. Hoppmann-Baum, M. Turner, and T. Koch. Controlling transient gas flow in real-world pipeline intersection areas. *Optimization and Engineering*, pages 1–48, 2020.
- [25] S. Hochreiter and J. Schmidhuber. Long short-term memory. *Neural computation*, 9(8):1735–1780, 1997.
- [26] K. Hoppmann, F. Hennings, R. Lenz, U. Gotzes, N. Heinecke, K. Spreckelsen, and T. Koch. Optimal operation of transient gas transport networks. Technical report, Technical Report 19-23, ZIB, Takustr. 7, 14195 Berlin, 2019.
- [27] D. P. Kingma and J. Ba. Adam: A method for stochastic optimization. *arXiv preprint arXiv:1412.6980*, 2014.
- [28] F. Kunz, M. Kendzioriski, W.-P. Schill, J. Weibezahn, J. Zepter, C. R. von Hirschhausen, P. Hauser, M. Zech, D. Möst, S. Heidari, et al. Electricity, heat, and gas sector data for modeling the german system. Technical report, DIW Data Documentation, 2017.

- [29] D. Masti and A. Bemporad. Learning binary warm starts for multiparametric mixed-integer quadratic programming. In *2019 18th European Control Conference (ECC)*, pages 1494–1499. IEEE, 2019.
- [30] M. MohamadiBaghmolaei, M. Mahmoudy, D. Jafari, R. MohamadiBaghmolaei, and F. Tabkhi. Assessing and optimization of pipeline system performance using intelligent systems. *Journal of Natural Gas Science and Engineering*, 18:64–76, 2014.
- [31] S. Moritz. *A mixed integer approach for the transient case of gas network optimization*. PhD thesis, Technische Universität, 2007.
- [32] V. Nair, S. Bartunov, F. Gimeno, I. von Glehn, P. Lichocki, I. Lobov, B. O’Donoghue, N. Sonnerat, C. Tjandraatmadja, P. Wang, R. Addanki, T. Hapuarachchi, T. Keck, J. Keeling, P. Kohli, I. Ktena, Y. Li, O. Vinyals, and Y. Zwols. Solving mixed integer programs using neural networks, 2020.
- [33] A. J. Osiadacz. Different Transient Flow Models - Limitations, Advantages, And Disadvantages. In *PSIG-9606*. Pipeline Simulation Interest Group, 1996.
- [34] A. Paszke, S. Gross, F. Massa, A. Lerer, J. Bradbury, G. Chanan, T. Killeen, Z. Lin, N. Gimelshein, L. Antiga, et al. Pytorch: An imperative style, high-performance deep learning library. In *Advances in neural information processing systems*, pages 8026–8037, 2019.
- [35] M. Petkovic, Y. Chen, I. Gamrath, U. Gotzes, N. S. Hadjidimitriou, J. Zittel, and T. Koch. A hybrid approach for high precision prediction of gas flows. Technical Report 19-26, ZIB, Takustr. 7, 14195 Berlin, 2019.
- [36] D. Pfau and O. Vinyals. Connecting generative adversarial networks and actor-critic methods. *arXiv preprint arXiv:1610.01945*, 2016.
- [37] A. Pourfard, H. Moetamedzadeh, R. Madoliat, and E. Khanmirza. Design of a neural network based predictive controller for natural gas pipelines in transient state. *Journal of Natural Gas Science and Engineering*, 62:275–293, 2019.
- [38] R. Z. Ríos-Mercado and C. Borraz-Sánchez. Optimization problems in natural gas transportation systems: A state-of-the-art review. *Applied Energy*, 147:536–555, 2015.
- [39] D. B. Rubin. The bayesian bootstrap. *The annals of statistics*, pages 130–134, 1981.
- [40] R. Ruiz, C. Maroto, and J. Alcaraz. A decision support system for a real vehicle routing problem. *European Journal of Operational Research*, 153(3):593–606, 2004.
- [41] L. N. Smith. Cyclical learning rates for training neural networks, 2017.

- [42] C. Szegedy, S. Ioffe, V. Vanhoucke, and A. A. Alemi. Inception-v4, inception-resnet and the impact of residual connections on learning. In *Thirty-first AAAI conference on artificial intelligence*, 2017.
- [43] Y. Tang, S. Agrawal, and Y. Faenza. Reinforcement learning for integer programming: Learning to cut. *arXiv preprint arXiv:1906.04859*, 2019.
- [44] P. S. Thomas and E. Brunskill. Policy gradient methods for reinforcement learning with function approximation and action-dependent baselines. *arXiv preprint arXiv:1706.06643*, 2017.
- [45] E. Wong and J. Z. Kolter. Provable defenses against adversarial examples via the convex outer adversarial polytope. *arXiv preprint arXiv:1711.00851*, 2017.
- [46] I. Yueksel Erguen, J. Zittel, Y. Wang, F. Hennings, and T. Koch. Lessons learned from gas network data preprocessing. Technical report, Technical Report 20-13, ZIB, Takustr. 7, 14195 Berlin, 2020.
- [47] G. Zarpellon, J. Jo, A. Lodi, and Y. Bengio. Parameterizing branch-and-bound search trees to learn branching policies. *arXiv preprint arXiv:2002.05120*, 2020.

A Appendix

Algorithm 8: Prepare Discriminator Training Data

Input: Neural network $\mathbb{N}_{\{\theta_1, \theta_2\}}$, labelled_data
Result: Data for training \mathbb{D}_{θ_2}
new_labelled_data = [] ;
for $i = 0$; $i < num_data_new$ **do**
 initial_state = Uniformly select from generated offline data ;
 flow_forecast, pressure_forecast = Boundary Prognosis Generator()^a;
 $\pi = (\text{flow_forecast}, \text{pressure_forecast}, \text{initial_state})$;
 $\hat{z}_1, \hat{f}(\mathbb{P}_{\pi}^{\hat{z}_1}) = \mathbb{N}_{\{\theta_1, \theta_2\}}(\pi)$;
 $f(\mathbb{P}_{\pi}^{\hat{z}_1}) = \text{solve } \mathbb{P}_{\pi}^{\hat{z}_1}$;
 new_labelled_data.append($\pi, \hat{z}_1, f(\mathbb{P}_{\pi}^{\hat{z}_1})$) ;
end
return concatenate(labelled_data[-num_data_old:], new_labelled_data)

^aSee Algorithm 1

Algorithm 9: Discriminator Pretraining

Input: Discriminator \mathbb{D}_{θ_2} , data
optimizer = Adam(learning_rate, weight_decay);
dataloader = DataLoader(data, batch_size, shuffle=True);
lr_scheduler=ReduceLRonPlateau();
for $i = 0; i < num_epochs$ **do**
 Discriminator Training Loop(\mathbb{D}_{θ_2} , dataloader, optimizer) ¹;
 lr_scheduler.step();
end

Algorithm 10: Discriminator Training Loop

Input: Discriminator \mathbb{D}_{θ_2} , dataloader, optimizer
for *batch in dataloader* **do**
 optimizer.zero_grad();
 $\hat{f}(\mathbb{P}_{\pi}^{z_1}) = \mathbb{D}_{\theta_2}$ (batch);
 loss = L1Loss($\hat{f}(\mathbb{P}_{\pi}^{z_1})$, $f(\mathbb{P}_{\pi}^{z_1})$);
 loss.backward();
 optimizer.step();
end

Algorithm 11: Generator Training

Input: Neural network $\mathbb{N}_{\{\theta_1, \theta_2\}}$
Result: Average loss in training
optimizer = Adam();
lr_scheduler=cyclicLR^a(max_lr, base_lr, step_size_up);
data = [] ;
for $i = 0; i < num_scenarios$ **do**
 initial_state = Uniformly select from generated offline data ;
 flow_forecast, pressure_forecast = Boundary Prognosis Generator()^b;
 $\pi = (\text{flow_forecast}, \text{pressure_forecast}, \text{initial_state})$;
 data.append(π) ;
end
dataloader = DataLoader(data, batch_size, shuffle=True);
for *batch in dataloader* **do**
 optimizer.zero_grad();
 losses = [];
 $\hat{z}_1, \hat{f}(\mathbb{P}_{\pi}^{\hat{z}_1}) = \mathbb{N}_{\{\theta_1, \theta_2\}}$ (batch);
 loss = L1Loss($\hat{f}(\mathbb{P}_{\pi}^{\hat{z}_1})$, 0);
 loss.backward();
 optimizer.step();
 lr_scheduler.step();
 losses.append(loss);
end
Result: mean(losses)

^aIntroduced by Smith in [41], see also pytorch.org/docs/stable/optim.html#torch.optim.lr_scheduler.CyclicLR.

^bSee Algorithm 1

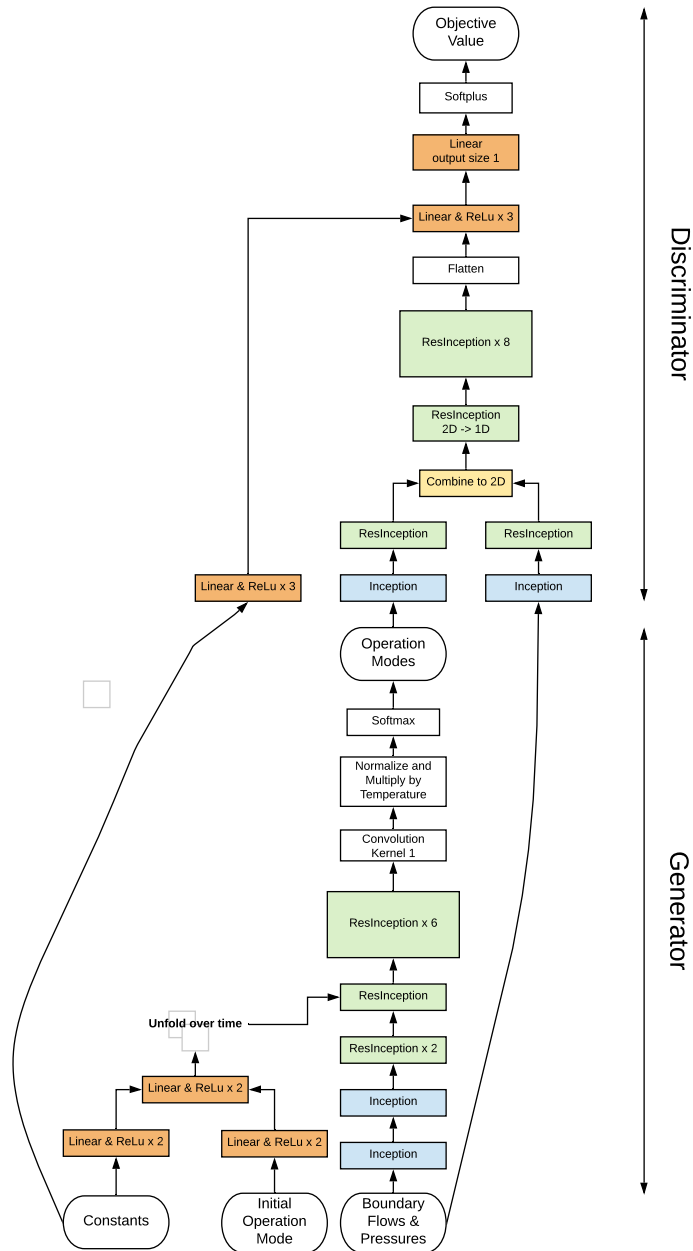


Figure 14: Neural Network Architecture

Parameter	Method	Value
batch_size	Algorithm 9	2048
num_epochs	Algorithm 9	500
learning_rate	Algorithm 9 / Adam	0.005
weight_decay	Algorithm 9 / Adam	5e-06
batch_size	Algorithm 11	2048
max_lr	Algorithm 11 / CyclicLR	0.0005
base_lr	Algorithm 11 / CyclicLR	5e-06
step_size_up	Algorithm 11 / CyclicLR	10000
num_scenarios	Algorithm 11	3200000
num_data_new	Algorithm 8	2048
num_data_old	Algorithm 8	8192
num_epochs	Algorithm 5	10
num_generator_epochs	Algorithm 5	25
num_discriminator_epochs	Algorithm 5	25
stopping_loss_discriminator	Algorithm 5	3 * 1022.5 ¹
stopping_loss_generator	Algorithm 5	0.9 * 121848.27 ²
num_prelabelled	Algorithm 5 / mix_in_prelabelled_data	8192
ratio_test	Algorithm 5 / split_data	0.1
learning_rate	Algorithm 5 / Adam	0.001
weight_decay	Algorithm 5 / Adam	5e-06
patience	Algorithm 5 / ReduceLROnPlateau	2
factor	Algorithm 5 / ReduceLROnPlateau	0.5

¹ 1022.5 was the test loss after initial discriminator training.

² 121848.27 represents the average $\hat{f}(\mathbb{P}_\pi^{\hat{z}_1})$ value over our artificial data.

Table 4: Parameters for training.

Parameter	Value
TimeLimit	3600 (s)
FeasibilityTol	1e-6
MIPGap	1e-4
MIPGapAbs	1e-2
NumericFocus	3

Table 5: Parameters for MIP solving.

	Parameters	Inception Blocks	Small Inception Blocks
Neural Network	1,701,505	13	12
Generator	1,165,576	13	0
Discriminator	535,929	0	12
Inception Block	87,296	-	-
Small Inception Block	27,936	-	-

Table 6: Number of parameters in the neural network and submodules.